

Sensitivity of He Flames in X-ray Bursts to Nuclear Physics

ZHI CHEN,¹ MICHAEL ZINGALE,¹ AND KIRAN EIDEN²

¹*Department of Physics and Astronomy, Stony Brook University, Stony Brook, NY 11794-3800, USA*

²*Department of Astronomy, University of California, Berkeley, Berkeley, CA 94720-3411, USA*

ABSTRACT

Through the use of axisymmetric 2D hydrodynamic simulations, we further investigate laterally propagating flames in X-ray bursts (XRBs). Our aim is to understand the sensitivity of a propagating helium flame to different nuclear physics. Using the *Castro* simulation code, we confirm the phenomenon of enhanced energy generation shortly after a flame is established after by adding $^{12}\text{C}(\text{p}, \gamma)^{13}\text{N}(\alpha, \text{p})^{16}\text{O}$ to the network, in agreement with the past literature. This sudden outburst of energy leads to a short accelerating phase, causing a drastic alteration in the overall dynamics of the flame in XRBs. Furthermore, we investigate the influence of different plasma screening routines on the propagation of the XRB flame. We finally examine the performance of simplified-SDC, a novel approach to hydrodynamics and reaction coupling incorporated in *Castro*, as an alternative to operator-splitting.

Keywords: convection—hydrodynamics—methods: numerical—stars: neutron—X-rays: bursts

1. INTRODUCTION

An X-ray burst (XRB) is a thermonuclear runaway caused by the ignition of the accreted fuel on the surface of a neutron star. Through Roche-lobe overflow, accreted matter is transferred from the companion star's envelope to the surface of the neutron star. The companion star is likely to have a similar composition to the Sun, i.e. a mixture of hydrogen, helium, and a small fraction of carbon, nitrogen, and oxygen (Galloway & Keek 2020). Nuclear explosions are directly affected by the initial composition of the accreted layer and the accretion rate. XRBs found with a mixture of hydrogen and helium fuel layers show bursts with ~ 5 sec rise time, while a pure helium layer is typically more explosive and shows bursts with shorter rise times (~ 1 sec). If the shell is enriched with carbon rather than helium, then the explosion is likely to have an extended rise duration, from minutes to hours known as a superburst (Kuulkers, E. 2002; Cumming & Bildsten 2001; Gupta et al. 2007).

Since the timescale of accretion between each burst is in the order of 10^4 secs while the rise time is in the order of $\sim 1 - 10$ sec (Parikh et al. 2013), it is unlikely for the same thermodynamic condition to exist on the entire surface of the neutron star and for the entire surface to start burning simultaneously (Shara 1982). Therefore, nuclear ignition is likely to begin in a localized region, and spread to the rest of the neutron star

(Spitkovsky et al. 2002). This asymmetrical burning leads to modulations in the observed flux during the rotation of neutron stars, which causes asymmetrical surface brightness during XRBs (Strohmayer et al. 2009). This explains burst oscillation behavior, a millisecond period variation of XRB intensity during rise time, and the double-peak light curve for non-photospheric-radius-expansion XRBs discovered and supported by observational data (Altamirano et al. 2010; Chakraborty & Bhattacharyya 2014; Bhattacharyya & Strohmayer 2006; Kaaret et al. 2007; Smith et al. 1997).

Numerous successful numerical simulations have explored the properties of neutron stars and XRBs. One-dimensional simulations can determine the nucleosynthesis, study the rp-process, estimate burst duration, and predict the light curve of XRBs by assuming spherical symmetry (Woosley et al. 2004b; Johnston et al. 2018; Meisel 2018; Johnston et al. 2020). On the other hand, multi-dimensional simulations are conducted to study the behavior of lateral flame propagation and flame structure for their nontrivial contributions to the structure of the XRB light curve (Eiden et al. 2020; Harpole et al. 2021; Cavecchi et al. 2013, 2015, 2016).

In our first work, Eiden et al. (2020), we studied the overall behavior of the burning front propagation using a 2D simulation with various approximations like artificially boosted flame speed and simple networks to minimize the computational cost, as well as high rotation rate to reduce the lateral flame length scale for greater flame confinement. In Harpole et al. (2021), we continued our work to explore the effect of rotation rate and crust temperature on flame propagation. We discovered that flame propagation was not greatly affected by the rotation rate, which is likely due to the balance between the confinement of the flame and the enhanced nuclear reaction rates caused by the increased rotation rate. It is also demonstrated that a cooler crust temperature drives a reduced flame speed and vice versa. Finally, in Zingale et al. (2023) we showed that 2D axisymmetric simulations compare well to full 3D simulations in capturing the nucleosynthesis of the early flame propagation. Continuing our work, we investigate the effects of different reaction networks, plasma screening methods, and time integration methods on the simulation of lateral flame propagation in XRBs.

2. NUMERICAL APPROACH

We use *Castro* (Almgren et al. 2010, 2020), an open-source, adaptive mesh, astrophysical simulation code, to perform all the simulations discussed in this manuscript. The reaction networks, integrators, equation of state (Timmes & Swesty 2000), thermal neutrino losses (Itoh et al. 1996), and conductivities Timmes (2000) are contained in the related *Microphysics* package (the *StarKiller Microphysics Development Team* et al. 2019).

Our simulation setup is the same as described in (Eiden et al. 2020; Harpole et al. 2021), so here we only reiterate the essential points. The simulations are performed using a 2D r - z cylindrical geometry, assuming azimuthal symmetry. The hydrodynamics is evolved using an unsplit piecewise parabolic method (Colella & Woodward 1984; Colella 1990; Miller & Colella 2002). We work with a corotating frame, and assume a rotational frequency $\Omega = 1000$ Hz for the neutron star. Gravity is assumed to be constant, since the accreted layer is thin. Our initial model is also unchanged from our previous papers. We employ a hydrostatic initial model to represent the neutron star's initial thermodynamic conditions, with a hot model in the left part of the domain and a cool model in the right—this drives a rightward propagating flame (a spreading hotspot for our geometry). By default, reactions are incorporated using operator-splitting.

This paper investigates the effect of reaction networks on the flame. We explore four different networks including a standard 13-isotope alpha chain as our reference network (see Sec. 2.1), two different plasma screening implementations (Sec. 2.2), and how the reactions and hydro are coupled together (Sec. 2.3).

2.1. Nuclear Reaction Networks

During an XRB, nucleosynthesis involves more than a thousand isotopes (Woosley et al. 2004b; Koike et al. 2004). However, due to computational constraints, most multi-dimensional simulations incorporate fewer than 20 isotopes. Thus, this paper aims to understand how the different approximations used in the nuclear physics impact on the lateral thermonuclear flame in XRBs.

2.1.1. `aprox13`

In Eiden et al. (2020); Harpole et al. (2021), we used the 13-isotope α -chain network, `aprox13` (Timmes 2019) network. We'll use that as the reference network for comparison here. The main feature of `aprox13` is the $(\alpha, p)(p, \gamma)$ approximation that eliminates the intermediate nuclei involved in $(\alpha, p)(p, \gamma)$ by assuming proton equilibrium in the reactive flow. As a result, `aprox13` has a total of 13 isotopes and 31 rates. Nevertheless, the $(\alpha, p)(p, \gamma)$ approximation can become less accurate for temperatures $\gtrsim 2.5 \times 10^9$ K, potentially affecting the energy generation rates. An illustration of this can be found in Smith et al. (2023) (see Figure 6 there).

As XRBs can reach temperatures close to the aforementioned limit ($T \gtrsim 2.5 \times 10^9$ K), it is important to understand if this approximation affects the flame. Therefore, we employ three more intricate networks, built with `pynucastro` using the latest rates from the REACLIB (Cyburt et al. 2010) library. These networks are described below.

2.1.2. `subch_full` and `subch_full_mod`

The `subch_full` network was introduced in Appendix B of Zingale et al. (2022) for simulating He burning in sub-Chandrasekhar mass white dwarfs (hence, the `subch` prefix). `subch_full` network has three main modifications compared to `aprox13` network. First `subch_full` explicitly includes the intermediate nuclei for the $(\alpha, p)(p, \gamma)$ sequence. Second, it has a better representation of carbon and oxygen burning by including the endpoint nuclei of the difference branches: $^{12}\text{C}(^{12}\text{C}, p)^{23}\text{Na}(p, \gamma)^{24}\text{Mg}$, $^{12}\text{C}(^{12}\text{C}, n)^{23}\text{Mg}(n, \gamma)^{24}\text{Mg}$, $^{16}\text{O}(^{16}\text{O}, n)^{31}\text{S}(n, \gamma)^{32}\text{S}$, and $^{16}\text{O}(^{12}\text{C}, n)^{27}\text{Si}(n, \gamma)^{28}\text{Si}$. Since the neutron capture processes on the intermediate nuclei happen at a fast timescale, the rates including neutrons are approximated by assuming the subsequent neutron capture is instantaneous as $^{12}\text{C}(^{12}\text{C}, \gamma)^{24}\text{Mg}$, $^{16}\text{O}(^{16}\text{O}, \gamma)^{32}\text{S}$, and $^{16}\text{O}(^{12}\text{C}, \gamma)^{28}\text{Si}$, and the network does not include neutrons. We also note that their reverse rates are not included due to their negligible effects at $T \sim 10^9$ K. Finally, we included the additional rates $^{14}\text{N}(\alpha, \gamma)^{18}\text{F}(\alpha, p)^{21}\text{Ne}$ and $^{12}\text{C}(p, \gamma)^{13}\text{N}(\alpha, p)^{16}\text{O}$, discussed in Shen & Bildsten (2009); Weinberg et al. (2006); Karakas et al. (2008); Fisker et al. (2008) to bypass the comparatively slow ^{12}C α -capture process, $^{12}\text{C}(\alpha, \gamma)^{16}\text{O}$, when $T \gtrsim 10^9$ K. The first α -capture process on ^{14}N and ^{18}F led to the production of protons that can be used for the α chain process on ^{12}C . When $T \gtrsim 10^9$ K, $^{12}\text{C}(p, \gamma)^{13}\text{N}(\alpha, p)^{16}\text{O}$ is expected to dominate the reactive flow towards the heavy α chain nuclei, which can lead to a completely different end-stage composition (Weinberg et al. 2006; Fisker et al. 2008). Since these additional rates leave ^{21}Ne as the endpoint, ^{22}Na is added to connect all the nuclei. With all the modifications, `subch_full` has 28 isotopes and 107 rates. Figure 1 shows a visualization of this network.

`subch_full_mod` is identical to the `subch_full` network, except that the $^{12}\text{C}(p, \gamma)^{13}\text{N}(\alpha, p)^{16}\text{O}$ and its reverse reactions are turned off. This is done to explore the significance of these two rates, as described in Shen & Bildsten (2009); Weinberg et al. (2006); Fisker et al. (2008).

2.1.3. `subch_simple`

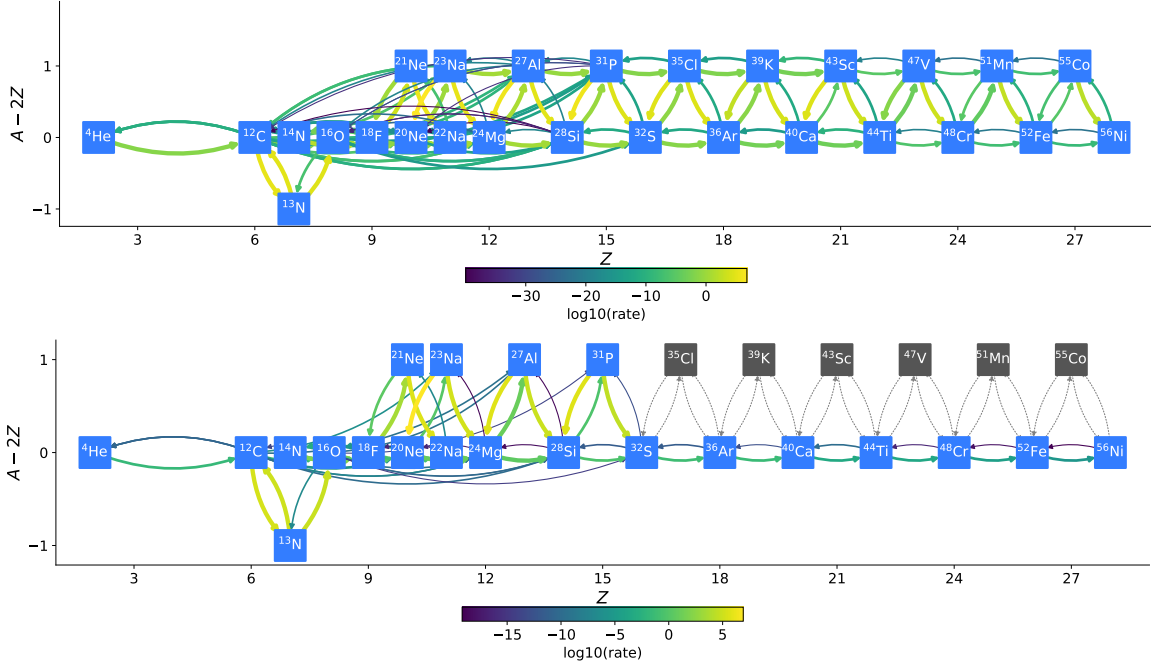


Figure 1. A simple visualization `subch_full` (top) and `subch_simple` (bottom) using the `pynucastro` package. The color bar shows the reaction rates with solar composition, $\rho = 10^6 \text{ g cm}^{-3}$, and $T = 2 \times 10^9 \text{ K}$. The horizontal axis shows the atomic number, Z , the vertical axis shows the extra number of neutrons compared to protons for the isotopes. The gray nodes and dotted gray lines represent the $(\alpha, p)(p, \gamma)$ approximation, which are not directly in the network. All reactions that have the form, $A(X, \alpha)B$ or $A(\alpha, X)B$, are hidden for better clarity.

Lastly, we present `subch_simple` network, a simplification of `subch_full` network that would resemble a more similar network to `aprox13`. The network omits a total of six nuclei, namely ^{35}Cl , ^{39}K , ^{43}Sc , ^{47}V , ^{51}Mn , and ^{55}Co , using the $(\alpha, p)(p, \gamma)$ approximation. The reverse rates of all $^{12}\text{C} + ^{12}\text{C}$, $^{16}\text{O} + ^{16}\text{O}$, and $^{16}\text{O} + ^{12}\text{C}$ are removed since they are not present in `aprox13`. All the forward and reverse rates of $^{12}\text{C} + ^{20}\text{Ne}$, $^{23}\text{Na}(\alpha, \gamma)^{27}\text{Al}$, and $^{27}\text{Al}(\alpha, \gamma)^{31}\text{P}$ are also removed to simplify the network. After the simplifications, we now have 22 isotopes and 57 rates. See the bottom panel of Figure 1 for visualization.

2.2. Plasma Screening Methods

Plasma screening is the enhancement of nuclear reaction rates due to the Coulomb coupling of the surrounding plasma electrons and ions. Plasma screening plays an important role in accurately calculating nuclear reaction rates in dense regions. Depending on the thermodynamic conditions, screening can enhance the rate by several orders of magnitude (see, e.g., Woosley et al. 2004a). There are many approximations for screening in the literature, but these are not often explored and compared in real simulations. We consider two different screening approximations for our XRB simulations.

A reaction rate cross section, σ , takes the form:

$$\sigma(E) = \frac{S(E)}{E} e^{-2\pi\eta} \quad (1)$$

where $S(E)$ contains the details of the nuclear physics, E is the energy of particle collisions in the center-of-mass frame, and η , accounts for Coulomb barrier penetration due to quantum effects (Newton et al. 2007). The reaction rate, R_{th} , is found by integrating the cross-section over the Maxwellian velocity distribution.

If the nuclei involved in the reaction are present in a high-density region that is permeated with plasma particles, then the strength of the Coulomb barrier would be reduced due to the plasma screening effect since the effective charge of the fusing nuclei are reduced. The screening enhancement factor is usually expressed as

$$F_{\text{scr}} = \exp(h) \quad (2)$$

where h is a function that characterizes the screening magnitude. Therefore, the overall screened nuclear reaction rate is defined as

$$R_{\text{scr}} = F_{\text{scr}} R_{\text{th}} \quad (3)$$

The plasma screening effect exhibits varying behavior depending on the specific thermodynamic conditions. In the thermonuclear burning regime present in XRBs, we can divide the plasma into weak and strong plasma screening regimes depending on the Coulomb coupling parameter of ions, Γ . A rough estimate is to consider weak plasma screening when $\Gamma \ll 1$ and strong plasma screening when $\Gamma \gtrsim 1$. In this manuscript, we explore and compare the effect of two different screening routines, SCREEN5 and CHUGUNOV2007, available in Microphysics on the spread of the lateral flame propagation in XRBs.

2.2.1. SCREEN5

SCREEN5 is the name of a widely-circulated screening routine (originally written in Fortran) that was the original screening routine used by Castro. The overall procedure of SCREEN5 is summarized in the appendix of Wallace et al. (1982). In SCREEN5, we define $\Gamma = (2/(Z_1 + Z_2))^{1/3} Z_1 Z_2 \Gamma_e$, where $\Gamma_e = e^2 \sqrt[3]{(4\pi n_e/3)}/(k_B T)$ describes the thermodynamic condition at which the reaction takes place, Z is the charge of the fusing nuclei, μ_{12} is the reduced mass for the two fusing nuclei, e is the electron charge, n_e is the electron number density, and k_B is Boltzmann's constant. When the plasma screening effect is weak or $\Gamma < 0.3$, SCREEN5 utilizes the equation proposed by Graboske et al. (1973); Dewitt et al. (1973), which assumes that the interacting nuclei are separated by zero distance. To account for the spatial dependence of the screening enhancement factor, a more precise description of the strong plasma screening limit is utilized when $\Gamma > 0.8$. In Jancovici (1977), a quadratic dependence of the separation distance between the interacting nuclei was shown. This idea was applied to a one-component plasma by Alastuey & Jancovici (1978a). By following a similar procedure outlined in Itoh et al. (1979), the screening routine for one-component plasma can be extended to a multi-component plasma, which is suitable for a general mixture of ions. Finally, in the intermediate screening regime, $0.3 < \Gamma < 0.8$, a weighted average between the weak and strong screening enhancement functions is used.

2.2.2. CHUGUNOV2007

The overall implementation of CHUGUNOV2007 screening routine follows Chugunov et al. (2007) with some modifications based on Yakovlev et al. (2006) to extend calculations in a one-component plasma to multi-component plasma. The screening function, h , proposed in Chugunov et al. (2007) used semi-classical calculations by assuming WKB Coulomb barrier penetration through the radial mean-field potential. Unlike SCREEN5 that uses separate expressions for different screening regimes, CHUGUNOV2007 employs a single expression that takes into account all screening limits up to $\Gamma \sim 600$. Additionally, we note that Microphysics includes other screening routines proposed by Chugunov & DeWitt (2009) and Chabrier & Potekhin (1998); Calder et al. (2007), although they are not covered in this discussion.

2.3. Time Evolution Methods

The default method for coupling hydrodynamics and nuclear reactions in **Castro** is the classic Strang-splitting method (Strang 1968). This operator-splitting approach considers the hydrodynamics and nuclear reactions to be independent processes. The overall procedure of Strang-splitting is as follows: first, the reactive part of the system is integrated over half of the timestep, $\Delta t/2$, using a standard ODE solver to determine the solution of an intermediate state, \mathcal{U}^* , which is centered in time. Advection then evolves \mathcal{U}^* through a full timestep Δt yielding the state \mathcal{U}^{**} . Finally, the second half-timestep of burning is done for $\Delta t/2$ starting with \mathcal{U}^{**} to obtain the final state \mathcal{U}^{n+1} . By applying the advection and hydrodynamic operator to an intermediate state that has already incorporated the nuclear reaction effect over $\Delta t/2$, an indirect coupling is achieved between the two operations and achieves a second-order accuracy in time. The Strang-splitting implementation in **Castro** was described in Zingale et al. (2021).

Spectral deferred correction (SDC) algorithms (Dutt et al. 2000; Bourlioux et al. 2003; Zingale et al. 2019) are iterative schemes for constructing higher-order accuracy solutions for ODEs by solving correction terms using low-order accuracy solvers like forward and backward Euler solvers. Correction terms are computed during each iteration to give improved solutions which are used as a source term in the next iteration. An arbitrarily high-order accuracy solution is then achieved after a series of correction sweeps.

A simplified-SDC algorithm was introduced in **Castro** in Zingale et al. (2022). The simplified-SDC algorithm explicitly couples reactions and hydrodynamics by including a reactive source in the hydrodynamics interface state prediction and including an advective source in the reaction ODE integration. The simplified-SDC scheme offers advantages over the traditional Strang-splitting method even though they both achieve second-order accuracy in time. Specifically, the simplified-SDC scheme provides a direct coupling between hydrodynamics and nuclear reactions, which eliminates the splitting error associated with operator splitting. It also reduces the stiffness of solving reaction equations, leading to reduced computational expenses under extreme thermodynamic conditions. In Zingale et al. (2022), it was observed that the simplified-SDC method provides a much more accurate evolution than the Strang-split method when evolving He and C detonations in white dwarfs.

3. SIMULATIONS AND RESULTS

We present a total of seven XRB simulations using different combinations of reaction networks, time evolution methods, and screening routines. In order to investigate the sensitivity of the propagating flame to nuclear reactions, the default screening routine, SCREEN5, and Strang-splitting are used with the four different networks: `aprox13`, `subch_full`, `subch_full_mod`, `subch_simple`. We replaced the SCREEN5 screening routine with CHUGUNOV2007 for the `aprox13` model with Strang-splitting to investigate the difference in their performance. Lastly, in order to test the performance of the simplified SDC method, we ran two additional simulations using `aprox13` and `subch_full` with simplified SDC instead of Strang-splitting. The overall summary of the simulations is shown in Table 1. We will refer to the simulations by the names in the table in the following discussion.

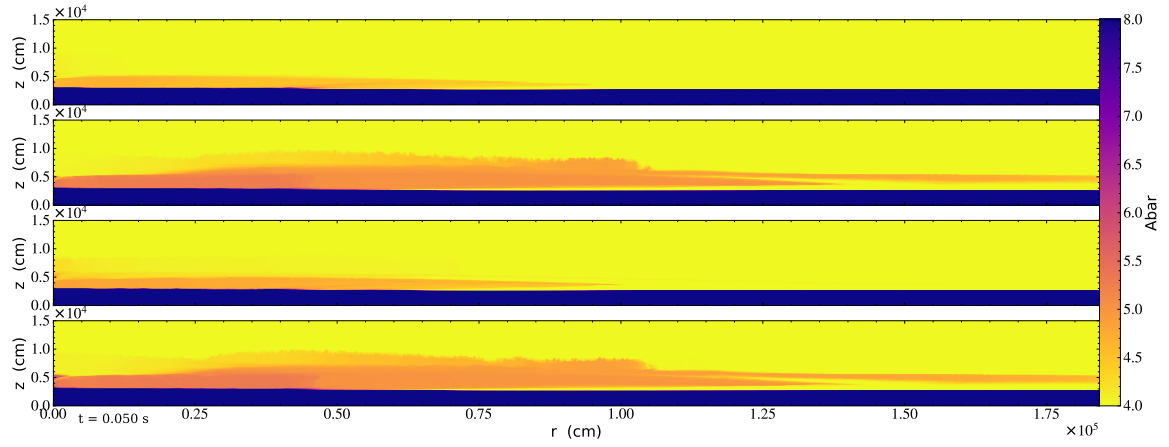
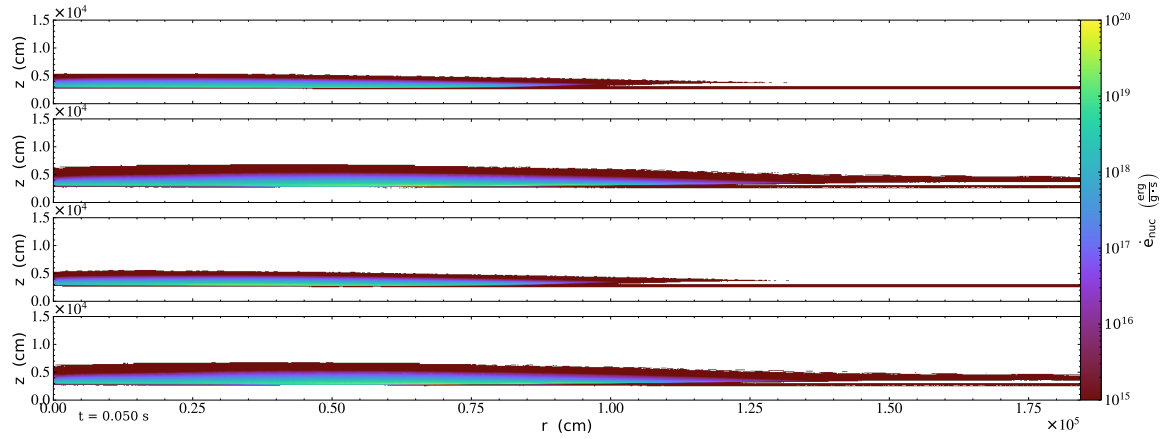
3.1. Reaction Network Comparison

3.1.1. Global behavior

Figure 2 shows a comparison of the mean molecular weight, \bar{A} , for the four networks at $t = 50$ ms. Regions with a larger \bar{A} represent the ash, tracing the burning in the accreted layer. One immediate feature is the similarity of the ash structure between `aprox13` and `subch_full_mod`, as well as between

Table 1. Various settings used for each simulation.

Name	Network	Integration	Screening
aprox13	aprox13	Strang-splitting	SCREEN5
subch_full	subch_full	Strang-splitting	SCREEN5
subch_full_mod	subch_full_mod	Strang-splitting	SCREEN5
subch_simple	subch_simple	Strang-splitting	SCREEN5
aprox13_sdc	aprox13	simplified SDC	SCREEN5
subch_full_sdc	subch_full	simplified SDC	SCREEN5
aprox13_chu	aprox13	Strang-splitting	CHUGUNOV2007

**Figure 2.** Slice plots comparing \bar{A} for aprox13 (top panel), subch_full (second panel from top), subch_full_mod (third panel), and subch_simple (last panel) at 50 ms.**Figure 3.** Slice plots comparing \dot{e}_{nuc} for aprox13 (top panel), subch_full (second panel from top), subch_full_mod (third panel), and subch_simple (last panel) at 50 ms.

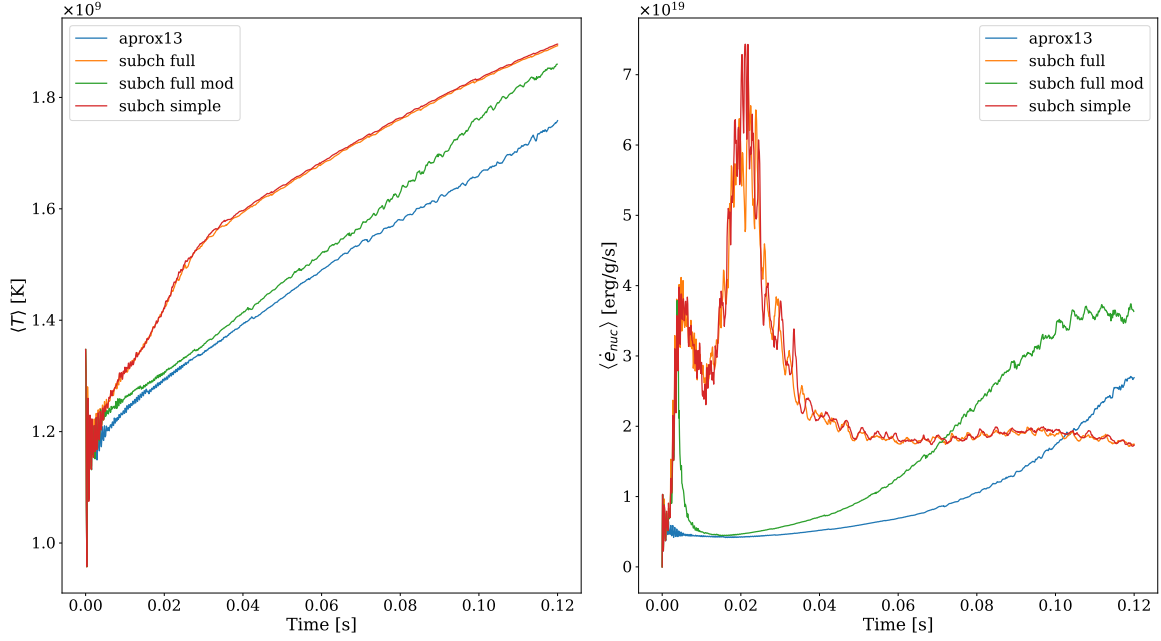


Figure 4. Time profiles showing the weighted temperature (left panel) and energy generation rate (right panel) of the burning front for the 4 simulations models: `aprox13`, `subch-full`, `subch-full-mod`, and `subch-simple`.

`subch-full` and `subch-simple`. For `subch-full` and `subch-simple`, there is a thicker overall ash structure on the surface indicating much more vigorous burning. The sudden increase in the ash height from $r = 5 \times 10^4$ cm to 10^5 cm for these two simulations further implies a non-uniform burning has taken place, unlike in `aprox13` and `subch-full-mod`. The darker color means that the ash in `subch-full` and `subch-simple` is composed of heavier nuclei suggesting a faster reactive flow burning to the heavier nuclei compared to the other two models. The ash also extends further out suggesting a faster flame speed compared to `aprox13` and `subch-full-mod`. The energy generation rate (shown in Figure 3) shows the same trends: `subch-full` and `subch-simple` clearly possess a higher \dot{e}_{nuc} in both magnitude and region coverage compared to the other two.

In order to quantify how the flame changes over time, we look at the density-weighted profile of temperature and energy generation rate in the burning, following the procedure in Harpole et al. (2021). We selected cells that are in the 99th percentile or higher for temperature or energy generation rate and compute a density-weighted average of temperature and energy generation rate:

$$\langle Q \rangle_w = \frac{\sum_{c_i} \rho(c_i) Q(c_i)}{\sum_{c_i} \rho(c_i)}; c_i \in C_{99}(Q) \quad (4)$$

where $\langle Q \rangle_w$ is the weighted quantity, $C_{99}(Q)$ are cells where the quantity, Q , is in the 99th percentile or higher, and $\rho(c_i)$ and $Q(c_i)$ are the density and the quantity in c_i cell. Figure 4 shows the resulting profiles.

The temperature and energy generation rate profiles for `subch-full` and `subch-simple` are nearly identical. As the primary distinction between these two is the $(\alpha, p)(p, \gamma)$ approximation for heavier nuclei, we can conclude that this approximation remains accurate in the context of XRB.

In general, there is no uniform shape in both T and \dot{e}_{nuc} for `subch-full` and `subch-simple`. After the flame-establishing phase at ~ 3 ms, there is a slight acceleration in temperature followed by a small decline,

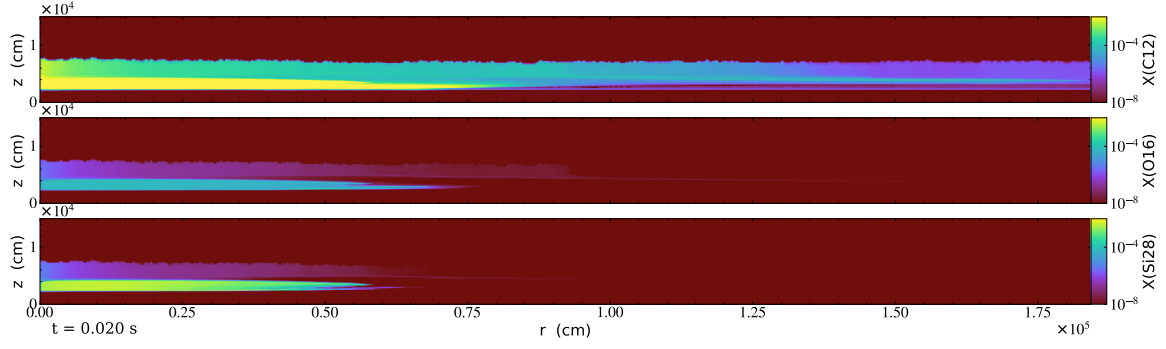


Figure 5. Slice plots showing the mass fractions of ^{12}C , ^{16}O , and ^{28}Si for `aprox13` at 20 ms.

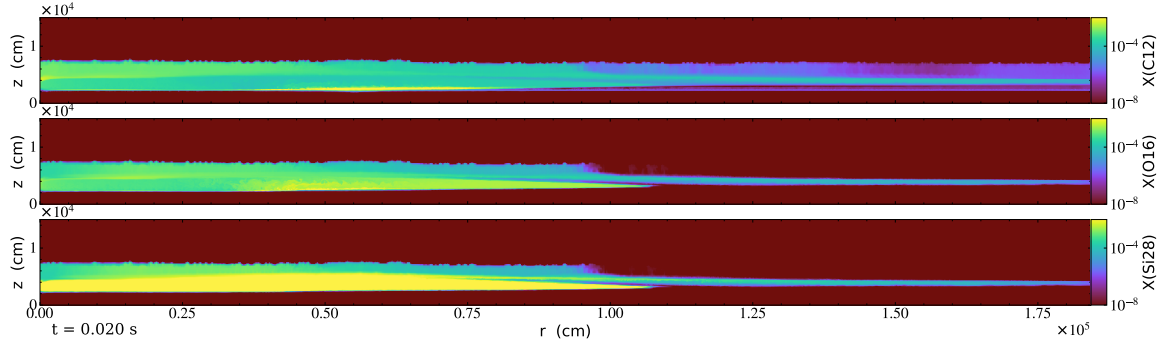


Figure 6. Slice plots showing the mass fractions of ^{12}C , ^{16}O , and ^{28}Si for `subch_full` at 20 ms.

corresponding to the first spike in \dot{e}_{nuc} . However, there is a sudden burst of energy production output from ~ 10 ms after the first spike for `subch_full` and `subch_simple`. The sudden spike in energy production in `subch_full`, as compared to `subch_full_mod`, is attributed to the inclusion of $^{12}\text{C}(p, \gamma)^{13}\text{N}(\alpha, p)^{16}\text{O}$ rates, as it is the only distinction between these two networks. By looking at the weighted \dot{e}_{nuc} profile, we determined that the burning acceleration phase had ended before 50 ms, as anticipated from previous slice plots. In general, the changes in \dot{e}_{nuc} are well reflected on the weighted-temperature profile.

Unlike `subch_full` or `subch_simple`, `aprox13` and `subch_full_mod` have a much more steady burning. Initially, `subch_full_mod` appears to keep pace with `subch_full` and `subch_simple`, but \dot{e}_{nuc} declines rapidly after reaching its peak following the flame-establishing phase. This is the consequence of the missing $^{12}\text{C}(p, \gamma)^{13}\text{N}(\alpha, p)^{16}\text{O}$, which puts a heavy limitation on the subsequent α -chain burning processes toward the heavy elements. However, \dot{e}_{nuc} for `subch_full_mod` gradually accelerates, reaching its peak at 120 ms similar to `aprox13`, but with a faster rate. In contrast, \dot{e}_{nuc} for `subch_full` and `subch_simple` gradually decrease during the later stages of burning after the burst.

3.1.2. Nucleosynthesis

In order to investigate the burning process in detail, Figure 5, 6, and 7 show the mass fractions of ^{12}C , ^{16}O , and ^{28}Si for `aprox13`, `subch_full`, and `subch_full_mod` at 20 ms, respectively. We exclude `subch_simple` due to its similarity to `subch_full`. For `aprox13`, all the burning products are concentrated in a thin region in the left of the domain, as we would expect given the high temperature behind the flame. Notably, there is an abundance of ^{12}C , as `aprox13` relies on the relatively slow α -capture rate

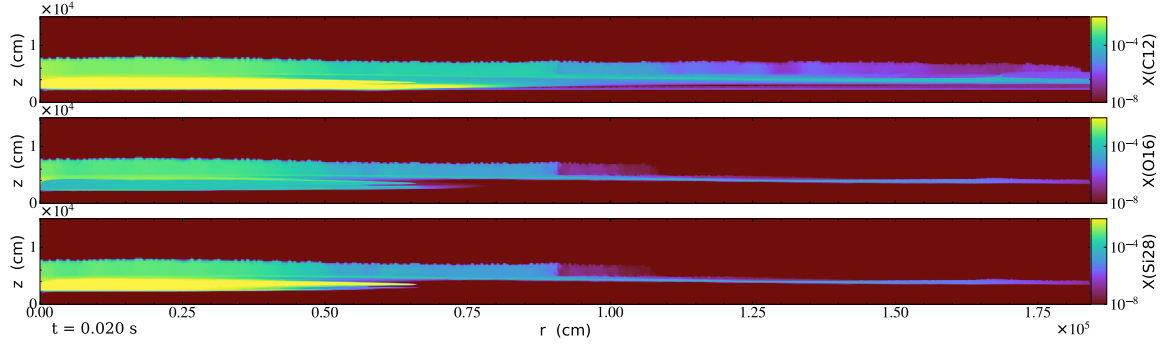


Figure 7. Slice plots showing the mass fractions of ^{12}C , ^{16}O , and ^{28}Si for subch_full_mod at 20 ms.

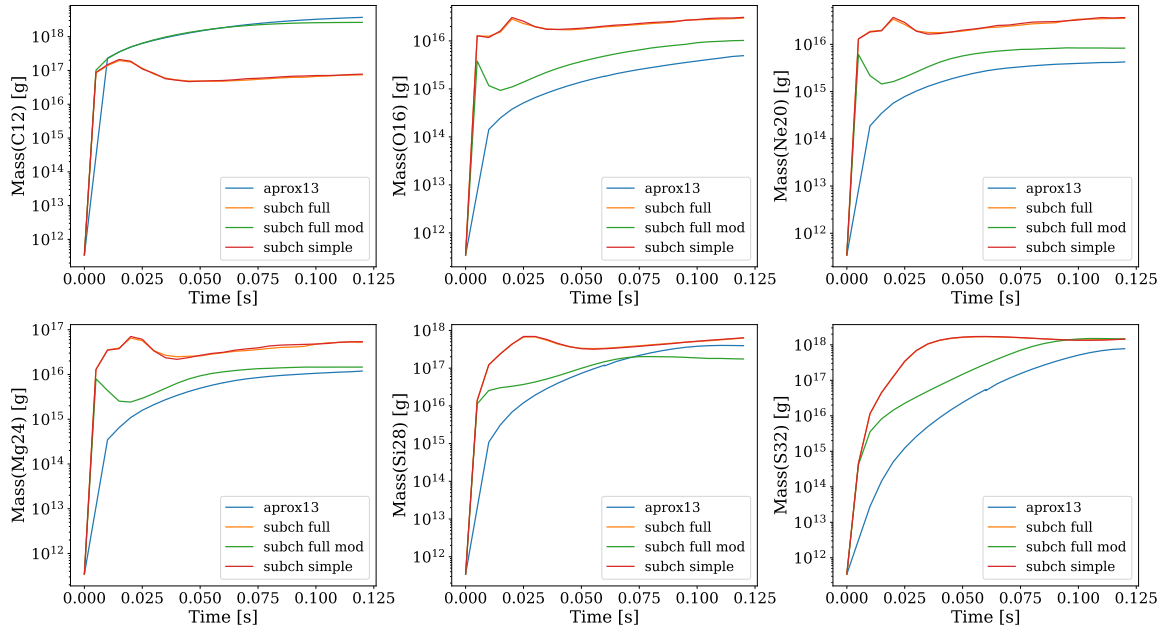


Figure 8. The overall evolution of the total mass for ^{12}C , ^{16}O , ^{20}Ne , ^{24}Mg , ^{28}Si , and ^{32}S for the 4 simulations models: aprox13, subch.full, subch.full.mod, and subch.simple.

to convert ^{12}C to ^{16}O . Additionally, ^{16}O is predominately transformed into ^{28}Si , which is the primary end product of the network.

With subch_full, we see that the ^{12}C is much more depleted in the burning region and there is much more production of heavy α chain isotopes through the α -chain, particularly ^{28}Si , at $t = 20$ ms. This phenomenon is consistent with the results of Weinberg et al. (2006); Fisker et al. (2008). The burning path, $^{12}\text{C}(p, \gamma)^{13}\text{N}(\alpha, p)^{16}\text{O}$, provides an efficient route for converting ^{12}C to ^{16}O compared to the α -capture rate.

Similar to aprox13, subch_full_mod exhibits a considerable amount of ^{12}C due to the absence of $^{12}\text{C}(p, \gamma)^{13}\text{N}(\alpha, p)^{16}\text{O}$ rate. However, unlike aprox13, a higher concentration of ^{16}O is observed in the upper vertical regions in subch_full_mod. This is likely the result of incorporating various additional rates, including more up-to-date rates from REACLIB library, in subch_full_mod compared to aprox13. Nevertheless, the quantity of ^{16}O in the bottom regions remains similar to those seen in aprox13, as the slightly higher temperature in the bottom region facilitates the burning of these fuels into ^{28}Si .

Figure 8 shows the total mass of the key α -chain isotopes to track their evolution. The initial spike in the production of ^{16}O , ^{20}Ne , ^{24}Mg , corresponds to the initial peak in energy generation rates for all subch networks shown in Figure 4. Although $^{12}\text{C}(\text{p}, \gamma)^{13}\text{N}(\alpha, \text{p})^{16}\text{O}$ efficiently burns ^{12}C into ^{16}O , resulting in a lower abundance of ^{12}C in `subch_full` and `subch_simple`, a considerable amount of ^{12}C still accumulates before $t \sim 18$ ms. Nevertheless, when $t \gtrsim 18$ ms, corresponding to $T \sim 1.3 \times 10^9$ K, the flow from ^{12}C to ^{16}O can surpass the triple- α process, resulting in a depletion of ^{12}C . This phenomenon is consistent with results in Weinberg & Bildsten (2007); Fisker et al. (2008). Consequently, there is an amplification in the nuclear energy generation rates and the mass production of heavy isotopes such as ^{28}Si . The early exhaustion of ^{12}C also causes a shortage of burning fuels during the subsequent burning stage for `subch_full` and `subch_simple`. This is because the nuclear burning process is now bottle-necked by the triple- α process, corresponding to an overall decline in the energy generation rate following the outburst. In contrast, both `aprox13` and `subch_full_mod` exhibit a continuous accumulation of ^{12}C since the networks are bottle-necked by the inefficient α -capture rate on ^{12}C to ^{16}O . However, unlike `aprox13`, `subch_full_mod` demonstrates slightly more effective burning paths for burning ^{12}C at $t \gtrsim 70$ ms. This phenomenon likely accelerates the overall nuclear burning process, resulting in significantly higher nuclear energy generation compared to `aprox13` during the late-stage burning, as shown in Figure 4.

3.1.3. Dynamics

Figure 9 shows the u - v phase plot (radial velocity vs. vertical velocity) for the four simulations models at $t = 25$ ms and $t = 100$ ms, colored by \dot{e}_{nuc} . Notably, the peak of the energy spike occurs at $t \sim 25$ ms for `subch_full` and `subch_simple`, resulting in the comparatively larger distribution in their u - v phase space plots. By 100 ms, the distribution appears to shrink considerably, likely due to decrease in the energy output as the flame is established. In contrast, the u - v phase space distribution for `aprox13` and `subch_full_mod` increased from $t = 25$ ms to $t = 100$ ms. However, there is one common feature slowly forming in the late stage where higher \dot{e}_{nuc} are preferably located in regions with a velocity opposite to the flame propagation. This a common feature observed in Eiden et al. (2020); Harpole et al. (2021).

To examine the overall impact of different reaction networks on the dynamics of the laterally propagating flame, Figure 10 shows the radial flame front position as a function of time. We follow the approach outlined in Eiden et al. (2020), where the position of the flame front is defined as the location at which \dot{e}_{nuc} of the 1D radial profile first drops to 0.1% of the global maximum \dot{e}_{nuc} for $r > r_{\text{max}}(\dot{e}_{\text{nuc}})$. As expected, `subch_full` and `subch_simple` have nearly identical burning front positions, with a sudden burst of acceleration followed by a gradual decline in velocity. These behaviors are consistent with the temperature and \dot{e}_{nuc} profiles we examined previously. On the other hand, `subch_full_mod` and `aprox13` exhibit a similar gradually accelerating burning front position, with a faster acceleration for `subch_full_mod`.

We fit the flame front position with a simple function to estimate the flame speed. For the `aprox13` and `subch_full_mod` networks, we use the same expression, Eq. 5, as in Harpole et al. (2021).

$$r(t) = \frac{1}{2}a_0t^2 + v_0t + r_0 \quad (5)$$

On the other hand, Eq. 6 is used for `subch_full` and `subch_simple` networks. A hyperbolic tangent function is added to the fitting function to account for the burst of acceleration at $10 \text{ ms} \lesssim t \lesssim 25 \text{ ms}$.

$$r(t) = A \tanh\left(\frac{t}{B} + C\right) + \frac{1}{2}a_0t^2 + v_0t + r_0 \quad (6)$$

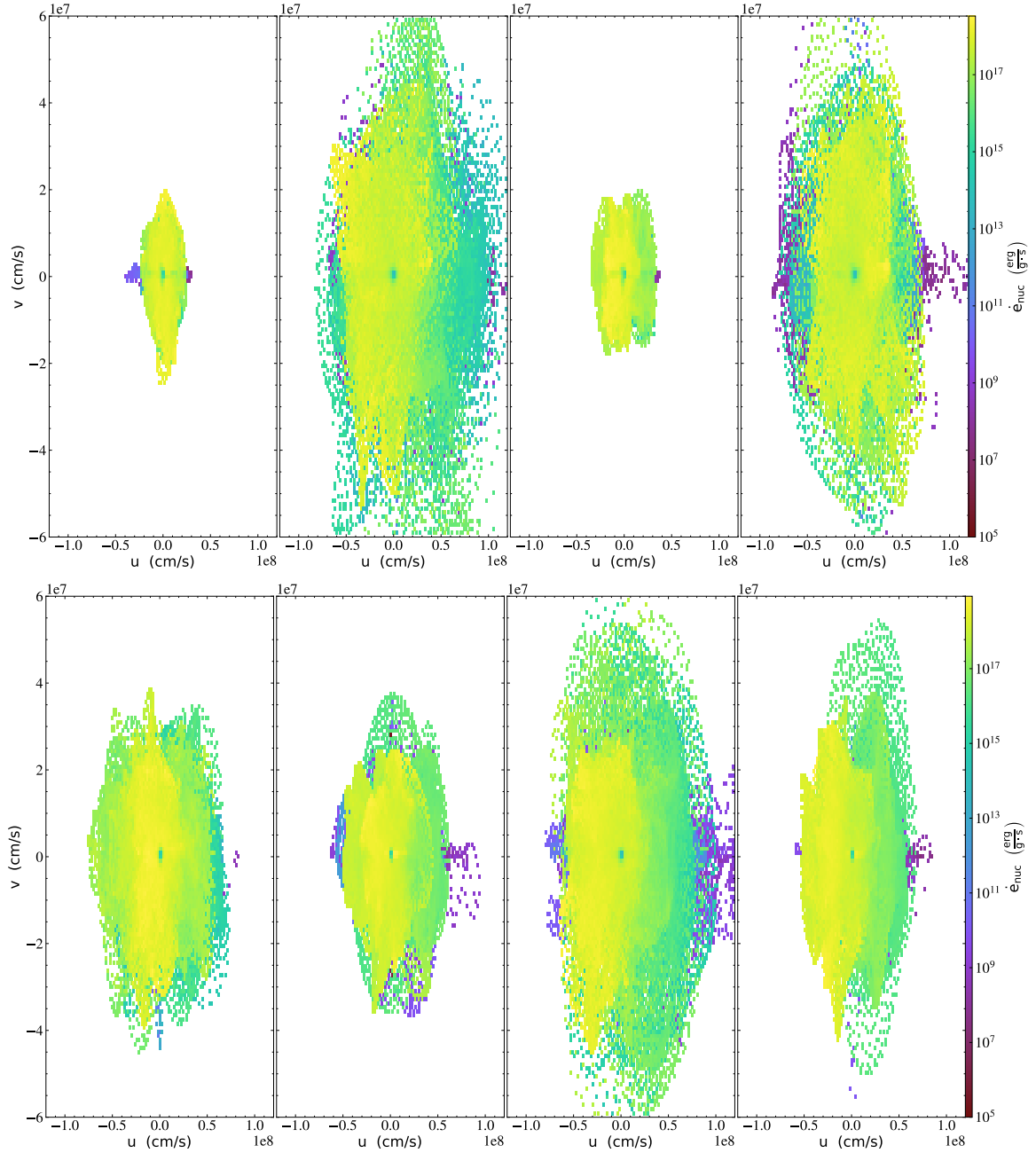


Figure 9. $u - v$ phase plots for `approx13` (panels in the first column on the left), `subch_full` (second column), `subch_full_mod` (third column), `subch_simple` (fourth column) at $t = 25$ ms (top 4 panels) and $t = 100$ ms (bottom 4 panels). The x-axis, u , shows the velocity in the r direction, whereas the y-axis, v , shows the velocity in the z direction. The color bar shows \dot{e}_{nuc} .

Both fitting functions are applied for $t > 8$ ms, and the fitted parameters along with their respective errors are shown in Table 2. The errors are calculated by taking the square root of the diagonal of the covariance matrix.

Using the fitted parameters, the instantaneous speed of the flame front at different times can be calculated, as shown in Table 3. We observe that during the acceleration burst phase at $t = 23$ ms, the difference in the instantaneous speed between `subch_full` and `subch_simple` can be as much as 7 times higher

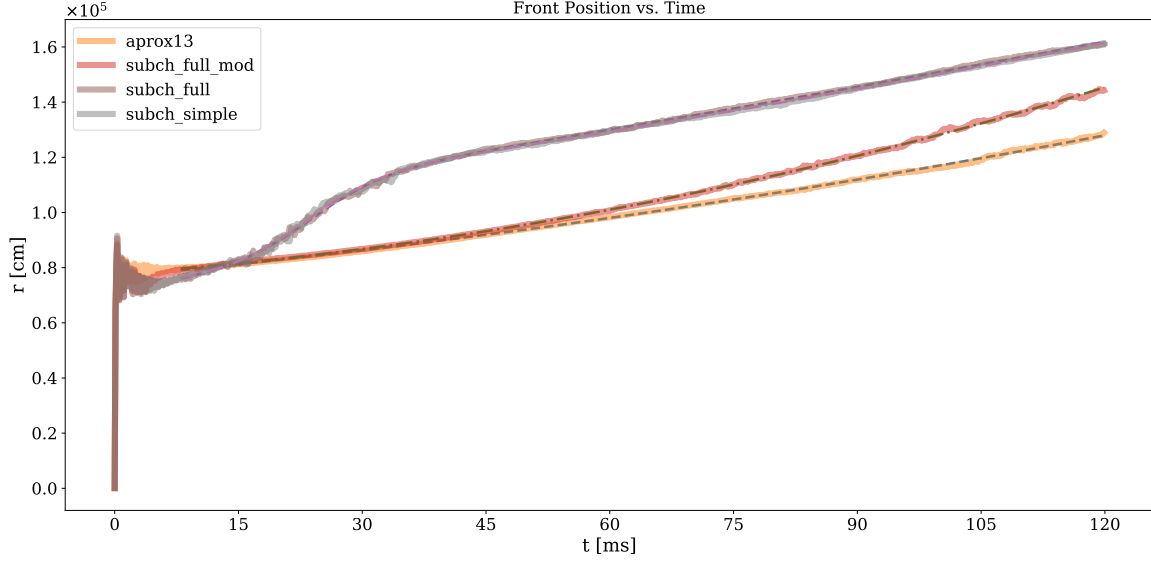


Figure 10. Flame front position as a function time for aprox13, subch_full, subch_full_mod, and subch_simple. The results of the fitting function, Eq. 5 and 6, is also shown in the dashed lines.

Table 2. Fitted parameters of the fitting functions Eq. 5 and 6 for aprox13, subch_full, subch_full_mod, and aprox13_chu. The fitting function is applied for $t > 8$ ms.

Name	a_0 [km s ⁻²]	v_0 [km s ⁻¹]	r_0 [km]	A [km]	B [s]	C
aprox13	24.22 ± 0.23	2.812 ± 0.015	0.7680 ± 0.0004	N/A	N/A	N/A
subch_full	9.22 ± 0.82	4.489 ± 0.067	0.8646 ± 0.0014	0.150 ± 0.001	0.0093 ± 0.0001	-2.551 ± 0.035
subch_full_mod	58.53 ± 0.24	2.122 ± 0.016	0.7773 ± 0.0004	N/A	N/A	N/A
subch_simple	15.60 ± 0.93	3.961 ± 0.076	0.8745 ± 0.0016	0.153 ± 0.002	0.0091 ± 0.0001	-2.575 ± 0.040
aprox13_chu	22.96 ± 0.20	2.578 ± 0.0133	0.7728 ± 0.0004	N/A	N/A	N/A

Table 3. Instantaneous flame propagation speed at $t = 23$ ms and $t = 100$ ms for aprox13, subch_full, subch_full_mod, subch_simple, and aprox13_chu. $t = 23$ ms and $t = 100$ ms represent the acceleration phase for subch_full and subch_simple and the steady phase at the late-stage, respectively. t_{10} represents the theoretical time for the flame to reach 10 km.

Name	v_{23} [km s ⁻¹]	v_{100} [km s ⁻¹]	t_{10} [s]
aprox13	3.369 ± 0.016	5.234 ± 0.027	0.7647
subch_full	20.732 ± 0.284	5.411 ± 0.105	0.9917
subch_full_mod	3.468 ± 0.017	7.975 ± 0.029	0.4873
subch_simple	21.095 ± 0.332	5.521 ± 0.120	0.8483
aprox13_chu	3.106 ± 0.014	4.874 ± 0.024	0.7912

compared to the other two simulations. Furthermore, subch_full_mod accelerates towards the end since it still has a sufficient amount of ¹²C fuel due to the inefficient reaction flows to ¹⁶O. Even though the flame front for subch_full_mod is expected to surpass subch_full and subch_simple at $t \sim 160$ ms,

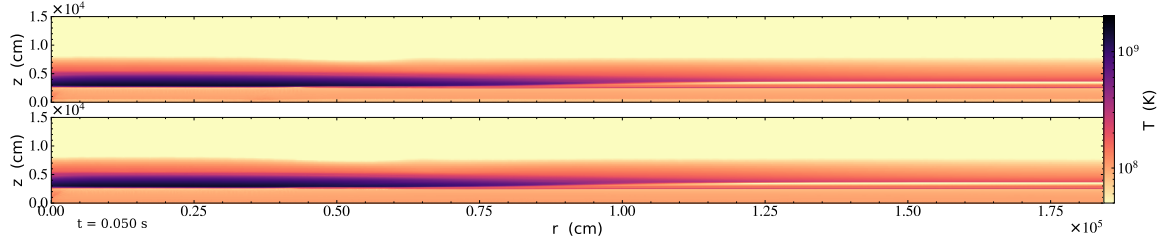


Figure 11. Slice plots comparing temperature for aprox13 (top panel) and aprox13_chu (bottom panel) at $t = 50$ ms.

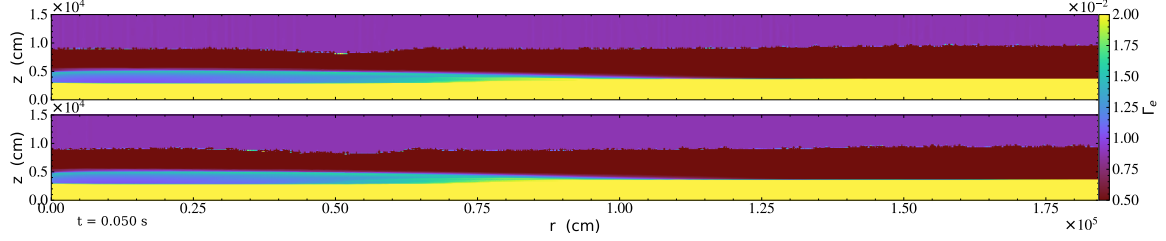


Figure 12. Slice plots comparing Γ_e for aprox13 (top panel) and aprox13_chu (bottom panel) at $t = 50$ ms.

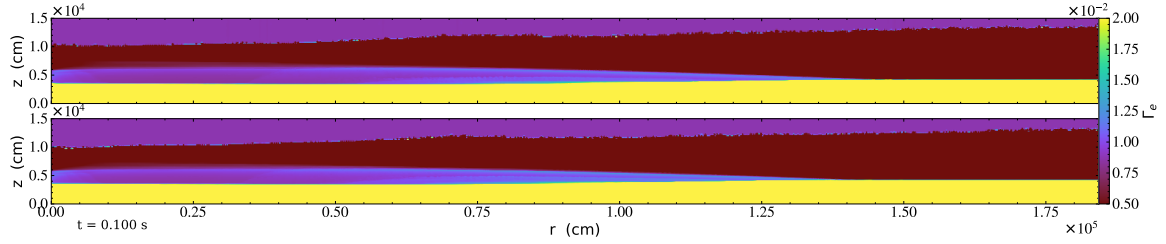


Figure 13. Slice plots comparing Γ_e for aprox13 (top panel) and aprox13_chu (bottom panel) at $t = 100$ ms.

based on Figure 10, \dot{e}_{nuc} from Figure 4 appears to reach its peak at 120 ms. Therefore, there is no guarantee that the lateral propagating flame for `subch_full_mod` would exceed its counterparts.

Assuming that the fitting functions accurately describe the flame propagation, the expected time for the flame to reach a typical neutron star radius of 10 km, t_{10} , can be calculated, as shown in Table 3. t_{10} serves as a rough prediction for the rise time of XRBs with a pure ${}^4\text{He}$ accretion layer. t_{10} for all models are $\lesssim 1$ sec, whereas t_{10} for `subch_full` is ~ 1 sec, consistent with previous observational studies (Galloway et al. 2008).

3.2. Plasma Screening Routine Comparison

We now present a comparison between the effects of SCREEN5 and CHUGUNOV2007 screening routines on the dynamics of the propagating flame in XRBs. Figure 11 shows the temperature for aprox13 and aprox13_chu at $t = 50$ ms, which suggests that there are no significant differences in the flame structure between the two models. Figure 12 and 13 show Γ_e , a measure to determine the approximate screening regime for the flame, at $t = 50$ ms and $t = 100$ ms.

Although a general trend of decreasing Γ_e is observed as the flame progress, it is noteworthy that there are more fusion processes involving heavier nuclei at later stages of burning. Assuming triple- α process, it can be inferred that the Coulomb coupling parameter, $\Gamma \sim 0.05$ and 0.025 for $t = 50$ ms and $t = 100$ ms.

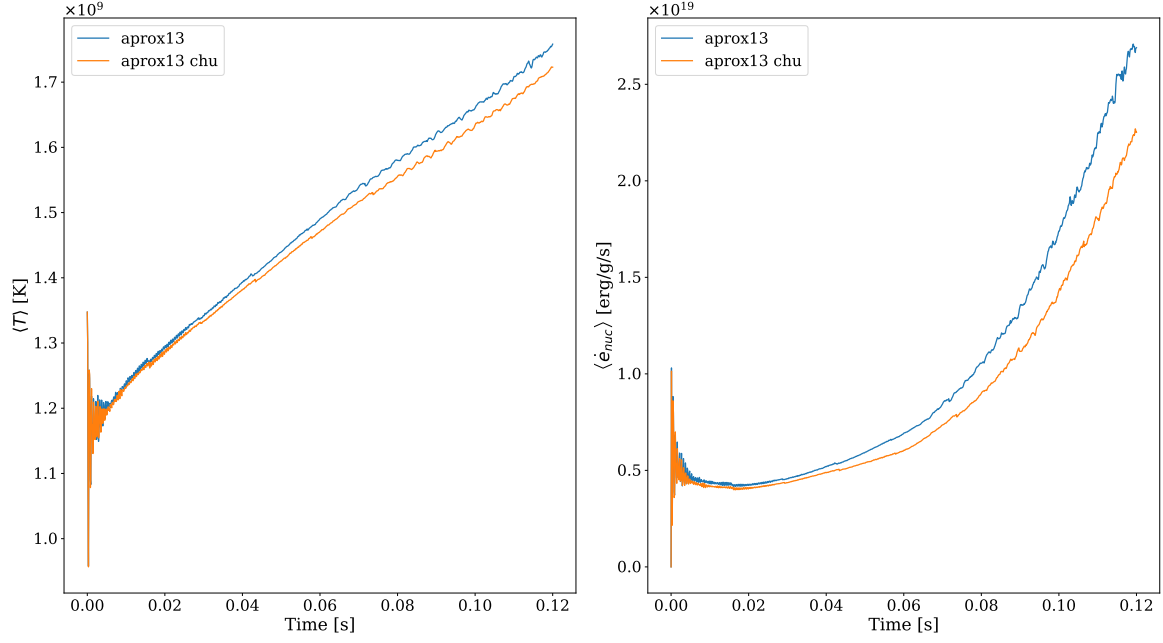


Figure 14. Time profiles showing the weighted temperature and energy generation rate of the burning front for aprox13 and aprox13_chu.

Meanwhile, for oxygen burning at $t = 50$ ms and 100 ms, $\Gamma \sim 0.48$ and 0.32, respectively. These results indicate that helium burning occurs in the weak screening regime, while heavier nuclei burning processes occur in the intermediate screening regime and gradually transition into the weak regime.

The comparison between aprox13 and aprox13_chu regarding the weighted temperature and energy generate rate is illustrated in Figure 14. This plot illustrates that overall the nuclear energy generation rate of aprox13 is higher and exhibits a faster increasing rate compared to aprox13_chu. At $t \sim 10$ ms, when the temperature of the two models are approximately equal, the difference in the nuclear energy generation rate indicates that SCREEN5 provides a stronger screening effect during the initial flame propagation phase compared to CHUGUNOV2007.

This finding is in agreement with the results from Chugunov et al. (2007), where it was shown that the screening effect calculated by Alastuey & Jancovici (1978b) is always greater than Chugunov et al. (2007) when $\Gamma \lesssim 40$ (See Figure 4 in Chugunov et al. (2007)). It should be emphasized that SCREEN5 uses calculation routines from Alastuey & Jancovici (1978b) to formulate the intermediate screening function along with the calculations from Graboske et al. (1973). Therefore, reactions that fall within the intermediate screening regime experience a slightly higher screening effect from SCREEN5 compared to CHUGUNOV2007. Consequently, the overall energy generation rates in the early time period are slightly higher for aprox13 compared to aprox13_chu. This phenomenon accelerates the increasing rate of temperature and the energy generation rate in the later stages of burning, amplifying the discrepancy between these two models as time progresses.

Figure 15 depicts the evolution of the flame front position over time. It is observed that the flame speed for aprox13_chu is slower compared to aprox13 due to the smaller value of \dot{e}_{nuc} at later times. However, the influence of the two screening methods on the overall flame dynamics is minimal. After fitting the data using Eq. 5, the fitted parameters and the instantaneous velocity at various times are shown in Table 2.

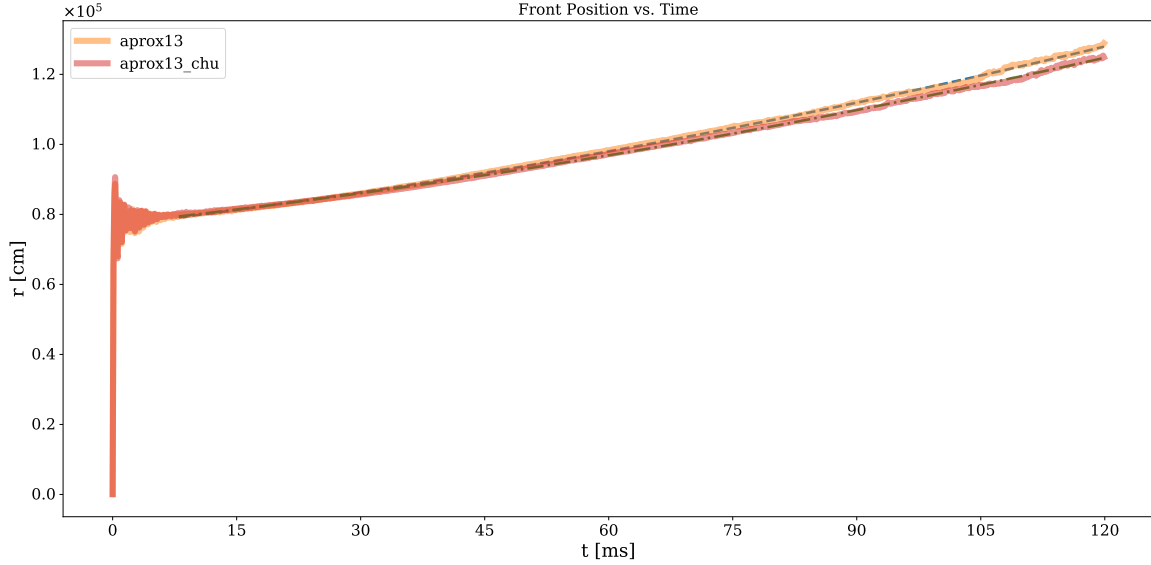


Figure 15. Flame front position as a function of time for `aprox13` and `aprox13_chu`. The dashed lines are the fitted curves using Eq. 5.

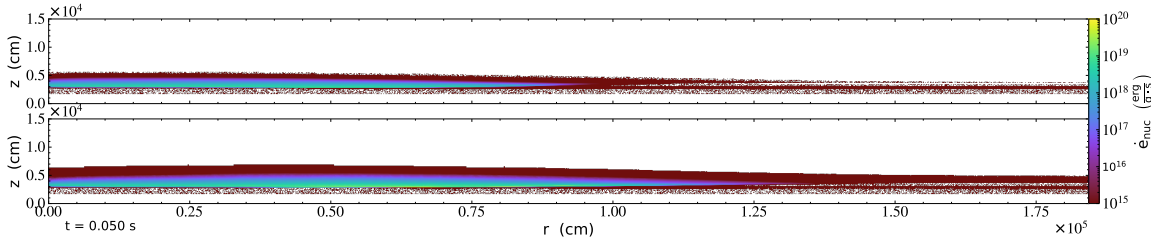


Figure 16. Slice plots comparing \dot{e}_{nuc} for `aprox13-sdc` (top panel) and `subch-full-sdc` (bottom panel) at $t = 50$ ms.

3.3. Time Evolution Method Comparison

Finally, we compare the simplified-SDC scheme with the traditional Strang-splitting. The overall results using the simplified-SDC scheme are nearly identical to the models that employed Strang-splitting. One consequence of the strong coupling between advection and reactions is, that to make the energy generation plot, we need to derive the nuclear energy release by subtracting off the advection contribution over a timestep. In regions where there is not much burning, roundoff error can introduce some noise into the energy generation plot, which is seen as the multiple dotted regions in the \dot{e}_{nuc} plot for `aprox13-sdc` and `subch-full-sdc`. This is simply an artifact of how we do the derivation.

The main advantage of the simplified-SDC integration lies in its stronger coupling between the reaction and hydrodynamics. This feature is demonstrated in the u - v phase plot for `aprox13-sdc` and `subch-full-sdc` (Figure 17). Comparing to the u - v phase plots for `aprox13` and `subch-full` at 100 ms (Figure 9), Figure 17 shows a smoother blend in the border of the regions with higher and lower \dot{e}_{nuc} , corresponding to negative and positive u , respectively. The smoother transition suggests this scheme is capable to resolve the flame in a volatile condition.

As shown in Zingale et al. (2022), in regions where the burning is vigorous, the simplified-SDC method provides a better solution than Strang splitting. However, the XRB flame we simulate here are not very

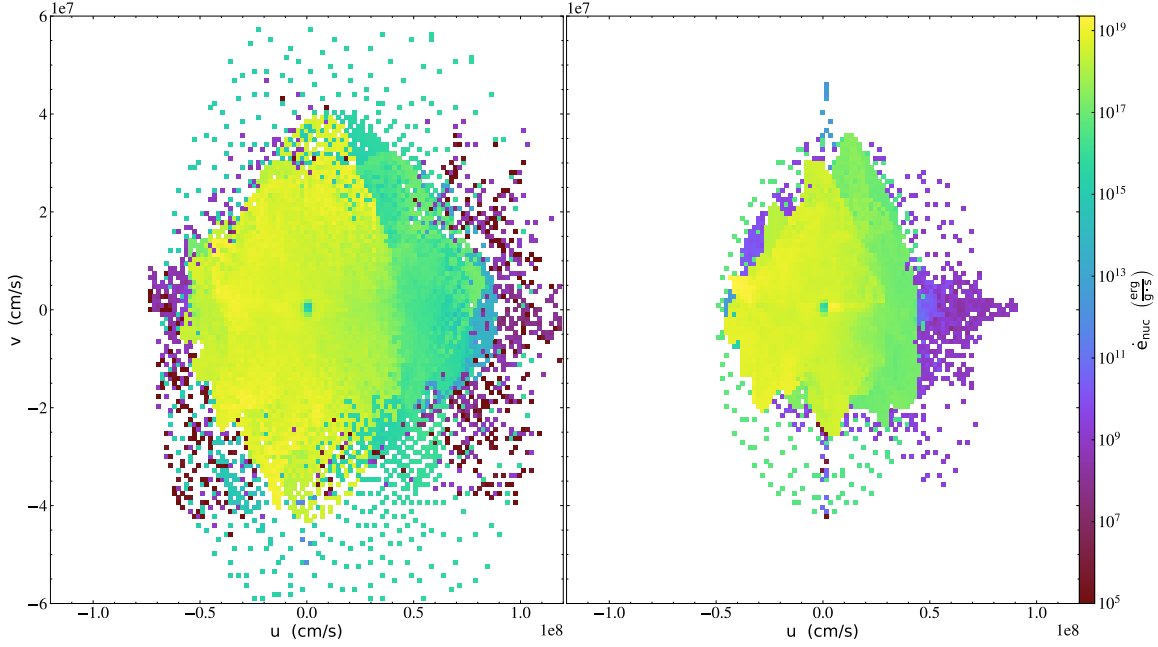


Figure 17. $u - v$ phase plots for `aprox13_sdc` (left panel) and `subch_full_sdc` (right panel) at $t = 100\text{ms}$.

demanding, so the benefit is minimal. As a result, the two simplified-SDC simulations were also more computationally-expensive than their Strang counterparts. This differs than the case in Zingale et al. (2022) where the simplified-SDC algorithm reduced computational expenses in extreme thermodynamic conditions by mitigating the stiffness of solving reaction equations.

4. SUMMARY

We explored the sensitivity of an XRB flame to the details of the nuclear physics: size of, and approximations in a reaction network, screening methods, and time-integration strategies. The main differences observed with reaction network are:

- The $(\alpha, p)(p, \gamma)$ approximation continues to be an accurate approach in simulating thermonuclear flames in XRBs. Up to $t = 120\text{ ms}$, the attained temperature during propagation of the thermonuclear flame is $\lesssim 2.5 \times 10^9\text{ K}$, and any minor errors associated with the approximation do not significantly affect the overall flame propagation. This conclusion is supported by the similar profiles observed between `subch_full` and `subch_simple` networks.
- The $^{12}\text{C}(p, \gamma)^{13}\text{N}(\alpha, p)^{16}\text{O}$ rates are critical in accurately modelling nuclear burning, nucleosynthesis, and flame propagation in XRBs. At $T \gtrsim 10^9\text{ K}$, these reactions dominate over the triple- α and the slow α capture processes from ^{12}C to ^{16}O . This allows an instant depletion of ^{12}C , leading to a burst of energy once the temperature reaches $\sim 1.3 \times 10^9\text{ K}$. This finding is consistent with the work of Weinberg et al. (2006), which claims a similar effect at $1.2 \times 10^9\text{ K}$. Upon incorporating these rates into the network, we have successfully simulated an accelerating phase for the laterally propagating flame.
- Even though there is not a significant difference between `aprox13` and `subch_full_mod`, `subch_full_mod` demonstrates an increasingly higher \dot{e}_{nuc} . Given that the $(\alpha, p)(p, \gamma)$ approximation is accurate, the additional rates must have gradually increased the overall \dot{e}_{nuc} in the long run.

Another possibility that caused the disparity between `subch_full_mod` and `aprox13` is the utilization of updated rates from REACLIB library in `subch_full_mod`, whereas `aprox13` didn't employ the most up-to-date rates. It is plausible that the contemporary adjustments made to the various reaction rates have contributed to the discrepancy between the two networks. However, further investigations are necessary to confirm this hypothesis.

- Among the four reaction networks used to simulate He flame propagation in XRBs, the `subch_simple` network proved to be the most effective. It is the smallest network that captures the initial acceleration of the propagating flame, which drastically alters the overall flame dynamics.

Comparing the two screening routines, `SCREEN5` and `CHUGUNOV2007`, we find that `CHUGUNOV2007` has a slightly weaker screening effect in the weak and intermediate screening regimes. As a consequence, the weaker screening effect from `CHUGUNOV2007` leads to a slightly slower flame compared to the `SCREEN5` model. This result matches our expectations and is in agreement with Chugunov et al. (2007).

Finally, we investigated the performance of the simplified-SDC scheme in comparison to the traditional Strang-splitting. For this problem, since the burning is not very vigorous, there is no strong benefit of using simplified-SDC over Strang-splitting.

Overall, this study gives us confidence that, by using the `subch_simple` network for our future simulations, we can accurately capture the dynamics of the flame. Our next step is to adapt the current simulation methodology to model a full star flame propagation model. A full star flame propagation simulation allows us to explore how flame dynamics changes subject to the geometric influence, such as the variations in Coriolis force. As the flame encounters the strongest Coriolis force at the pole and the weakest at the equator, its behavior can alter significantly depending on its position. Additionally, a full star simulation provides a more precise estimate of the time required for the flame to engulf the neutron star, which serves as a better approximation of the XRB's rise time.

Castro is open-source and freely available at <http://github.com/AMReX-Astro/Castro>. The work at Stony Brook was supported by DOE/Office of Nuclear Physics grant DE-FG02-87ER40317. This research was supported by the Exascale Computing Project (17-SC-20-SC), a collaborative effort of the U.S. Department of Energy Office of Science and the National Nuclear Security Administration. This research used resources of the National Energy Research Scientific Computing Center, a DOE Office of Science User Facility supported by the Office of Science of the U. S. Department of Energy under Contract No. DE-AC02-05CH11231. This research used resources of the Oak Ridge Leadership Computing Facility at the Oak Ridge National Laboratory, which is supported by the Office of Science of the U.S. Department of Energy under Contract No. DE-AC05-00OR22725, awarded through the DOE INCITE program. We thank NVIDIA Corporation for the donation of a Titan X and Titan V GPU through their academic grant program. This research has made use of NASA's Astrophysics Data System Bibliographic Services.

Facilities: NERSC, OLCF

Software: AMReX (Zhang et al. 2019), Castro (Almgren et al. 2010), GCC (<https://gcc.gnu.org/>), linux (<https://www.kernel.org/>), matplotlib (Hunter 2007, <http://matplotlib.org/>), NumPy (Oliphant 2007; van der Walt et al. 2011), python (<https://www.python.org/>), valgrind (Nethercote & Seward 2007), VODE (Brown

et al. 1989), yt (Turk et al. 2010) pynucastro (E. Willcox & Zingale 2018; Smith et al. 2023; the pynucastro development et al. 2022)

REFERENCES

- Alastuey, A., & Jancovici, B. 1978a, *ApJ*, 226, 1034, doi: [10.1086/156681](https://doi.org/10.1086/156681)
- . 1978b, *ApJ*, 226, 1034, doi: [10.1086/156681](https://doi.org/10.1086/156681)
- Almgren, A., Sazo, M. B., Bell, J., et al. 2020, *Journal of Open Source Software*, 5, 2513, doi: [10.21105/joss.02513](https://doi.org/10.21105/joss.02513)
- Almgren, A. S., Beckner, V. E., Bell, J. B., et al. 2010, *ApJ*, 715, 1221, doi: [10.1088/0004-637x/715/2/1221](https://doi.org/10.1088/0004-637x/715/2/1221)
- Altamirano, D., Watts, A., Linares, M., et al. 2010, *Monthly Notices of the Royal Astronomical Society*, 409, 1136, doi: [10.1111/j.1365-2966.2010.17369.x](https://doi.org/10.1111/j.1365-2966.2010.17369.x)
- Bhattacharyya, S., & Strohmayer, T. E. 2006, *The Astrophysical Journal*, 636, L121, doi: [10.1086/500199](https://doi.org/10.1086/500199)
- Bourlioux, A., Layton, A. T., & Minion, M. L. 2003, *Journal of Computational Physics*, 189, 651
- Brown, P. N., Byrne, G. D., & Hindmarsh, A. C. 1989, *SIAM J. Sci. and Stat. Comput.*, 10, 1038, doi: [10.1137/0910062](https://doi.org/10.1137/0910062)
- Calder, A. C., Townsley, D. M., Seitzzahl, I. R., et al. 2007, *The Astrophysical Journal*, 656, 313, doi: [10.1086/510709](https://doi.org/10.1086/510709)
- Cavecchi, Y., Levin, Y., Watts, A. L., & Braithwaite, J. 2016, *Monthly Notices of the Royal Astronomical Society*, 459, 1259, doi: [10.1093/mnras/stw728](https://doi.org/10.1093/mnras/stw728)
- Cavecchi, Y., Watts, A. L., Braithwaite, J., & Levin, Y. 2013, *Mon. Not. R. Astron. Soc.*, 434, 3526, doi: [10.1093/mnras/stt1273](https://doi.org/10.1093/mnras/stt1273)
- Cavecchi, Y., Watts, A. L., Levin, Y., & Braithwaite, J. 2015, *Monthly Notices of the Royal Astronomical Society*, 448, 445, doi: [10.1093/mnras/stu2764](https://doi.org/10.1093/mnras/stu2764)
- Chabrier, G., & Potekhin, A. Y. 1998, *Physical Review E*, 58, 4941, doi: [10.1103/physreve.58.4941](https://doi.org/10.1103/physreve.58.4941)
- Chakraborty, M., & Bhattacharyya, S. 2014, *The Astrophysical Journal*, 792, 4, doi: [10.1088/0004-637x/792/1/4](https://doi.org/10.1088/0004-637x/792/1/4)
- Chugunov, A. I., & DeWitt, H. E. 2009, *Physical Review C*, 80, doi: [10.1103/physrevc.80.014611](https://doi.org/10.1103/physrevc.80.014611)
- Chugunov, A. I., DeWitt, H. E., & Yakovlev, D. G. 2007, *Physical Review D*, 76, doi: [10.1103/physrevd.76.025028](https://doi.org/10.1103/physrevd.76.025028)
- Colella, P. 1990, *J. Comput. Phys.*, 87, 171, doi: [10.1016/0021-9991\(90\)90233-q](https://doi.org/10.1016/0021-9991(90)90233-q)
- Colella, P., & Woodward, P. R. 1984, *J. Comput. Phys.*, 54, 174, doi: [10.1016/0021-9991\(84\)90143-8](https://doi.org/10.1016/0021-9991(84)90143-8)
- Cumming, A., & Bildsten, L. 2001, *The Astrophysical Journal*, 559, L127, doi: [10.1086/323937](https://doi.org/10.1086/323937)
- Cyburt, R. H., Amthor, A. M., Ferguson, R., et al. 2010, *ApJS*, 189, 240, doi: [10.1088/0067-0049/189/1/240](https://doi.org/10.1088/0067-0049/189/1/240)
- Dewitt, H. E., Graboske, H. C., & Cooper, M. S. 1973, *ApJ*, 181, 439, doi: [10.1086/152061](https://doi.org/10.1086/152061)
- Dutt, A., Greengard, L., & Rokhlin, V. 2000, *BIT Numerical Mathematics*, 40, 241
- E. Willcox, D., & Zingale, M. 2018, *JOSS*, 3, 588, doi: [10.21105/joss.00588](https://doi.org/10.21105/joss.00588)
- Eiden, K., Zingale, M., Harpole, A., et al. 2020, *ApJ*, 894, 6, doi: [10.3847/1538-4357/ab80bc](https://doi.org/10.3847/1538-4357/ab80bc)
- Fisker, J. L., Schatz, H., & Thielemann, F. 2008, *ASTROPHYS J SUPPL S*, 174, 261, doi: [10.1086/521104](https://doi.org/10.1086/521104)
- Galloway, D. K., & Keek, L. 2020, in *Timing Neutron Stars: Pulsations, Oscillations and Explosions* (Springer Berlin Heidelberg), 209–262, doi: [10.1007/978-3-662-62110-3_5](https://doi.org/10.1007/978-3-662-62110-3_5)
- Galloway, D. K., Muno, M. P., Hartman, J. M., Psaltis, D., & Chakraborty, D. 2008, *Astrophysical Journal Supplement Series*, The, 179, 360, doi: [10.1086/592044](https://doi.org/10.1086/592044)
- Graboske, H. C., Dewitt, H. E., Grossman, A. S., & Cooper, M. S. 1973, *ApJ*, 181, 457, doi: [10.1086/152062](https://doi.org/10.1086/152062)
- Gupta, S., Brown, E. F., Schatz, H., Moller, P., & Kratz, K.-L. 2007, *The Astrophysical Journal*, 662, 1188, doi: [10.1086/517869](https://doi.org/10.1086/517869)
- Harpole, A., Ford, N. M., Eiden, K., et al. 2021, *ApJ*, 912, 36, doi: [10.3847/1538-4357/abee87](https://doi.org/10.3847/1538-4357/abee87)
- Hunter, J. D. 2007, *Comput. Sci. Eng.*, 9, 90, doi: [10.1109/mcse.2007.55](https://doi.org/10.1109/mcse.2007.55)
- Itoh, N., Hayashi, H., Nishikawa, A., & Kohyama, Y. 1996, *ApJS*, 102, 411, doi: [10.1086/192264](https://doi.org/10.1086/192264)
- Itoh, N., Totsuji, H., Ichimaru, S., & Dewitt, H. E. 1979, *ApJ*, 234, 1079, doi: [10.1086/157590](https://doi.org/10.1086/157590)
- Jancovici, B. 1977, *Journal of Statistical Physics*, 17, 357

- Johnston, Z., Heger, A., & Galloway, D. K. 2018, Monthly Notices of the Royal Astronomical Society, 477, 2112, doi: [10.1093/mnras/sty757](https://doi.org/10.1093/mnras/sty757)
- . 2020, Monthly Notices of the Royal Astronomical Society, 494, 4576, doi: [10.1093/mnras/staa1054](https://doi.org/10.1093/mnras/staa1054)
- Kaaret, P., Prieskorn, Z., in 't Zand, J. J. M., et al. 2007, The Astrophysical Journal, 657, L97, doi: [10.1086/513270](https://doi.org/10.1086/513270)
- Karakas, A. I., Lee, H. Y., Lugaro, M., Görres, J., & Wiescher, M. 2008, The Astrophysical Journal, 676, 1254, doi: [10.1086/528840](https://doi.org/10.1086/528840)
- Koike, O., aki Hashimoto, M., Kuromizu, R., & ichirou Fujimoto, S. 2004, The Astrophysical Journal, 603, 242, doi: [10.1086/381354](https://doi.org/10.1086/381354)
- Kuulkers, E. 2002, A&A, 383, L5, doi: [10.1051/0004-6361:20011811](https://doi.org/10.1051/0004-6361:20011811)
- Meisel, Z. 2018, The Astrophysical Journal, 860, 147, doi: [10.3847/1538-4357/aac3d3](https://doi.org/10.3847/1538-4357/aac3d3)
- Miller, G., & Colella, P. 2002, J. Comput. Phys., 183, 26, doi: [10.1006/jcph.2002.7158](https://doi.org/10.1006/jcph.2002.7158)
- Nethercote, N., & Seward, J. 2007, in Proceedings of the 2007 ACM SIGPLAN conference on Programming language design and implementation - PLDI '07, PLDI '07 (New York, NY, USA: ACM Press), 89–100, doi: [10.1145/1250734.1250746](https://doi.org/10.1145/1250734.1250746)
- Newton, J. R., Iliadis, C., Champagne, A. E., et al. 2007, Phys. Rev. C, 75, 045801, doi: [10.1103/PhysRevC.75.045801](https://doi.org/10.1103/PhysRevC.75.045801)
- Oliphant, T. E. 2007, Comput. Sci. Eng., 9, 10, doi: [10.1109/mcse.2007.58](https://doi.org/10.1109/mcse.2007.58)
- Parikh, A., José, J., Sala, G., & Iliadis, C. 2013, Progress in Particle and Nuclear Physics, 69, 225, doi: [10.1016/j.pnpnp.2012.11.002](https://doi.org/10.1016/j.pnpnp.2012.11.002)
- Shara, M. M. 1982, ApJ, 261, 649, doi: [10.1086/160376](https://doi.org/10.1086/160376)
- Shen, K. J., & Bildsten, L. 2009, The Astrophysical Journal, 699, 1365, doi: [10.1088/0004-637x/699/2/1365](https://doi.org/10.1088/0004-637x/699/2/1365)
- Smith, A. I., Johnson, E. T., Chen, Z., et al. 2023, The Astrophysical Journal, 947, 65, doi: [10.3847/1538-4357/acbaff](https://doi.org/10.3847/1538-4357/acbaff)
- Smith, D. A., Morgan, E. H., & Bradt, H. 1997, The Astrophysical Journal, 479, L137, doi: [10.1086/310604](https://doi.org/10.1086/310604)
- Spitkovsky, A., Levin, Y., & Ushomirsky, G. 2002, The Astrophysical Journal, 566, 1018, doi: [10.1086/338040](https://doi.org/10.1086/338040)
- Strang, G. 1968, SIAM J. Numer. Anal., 5, 506, doi: [10.1137/0705041](https://doi.org/10.1137/0705041)
- Strohmayer, E., Zhang, W., Swank, H., et al. 2009, The Astrophysical Journal Letters, 469, L9, doi: [10.1086/310261](https://doi.org/10.1086/310261)
- the pynucastro development, Boyd, B., Cao, L., et al. 2022, pynucastro/pynucastro: pynucastro 2.0.2, 2.0.2, Zenodo, doi: [10.5281/zenodo.7239007](https://doi.org/10.5281/zenodo.7239007)
- the StarKiller Microphysics Development Team, Bishop, A., Fields, C. E., et al. 2019, starkiller-astro/Microphysics: 19.04, doi: [10.5281/zenodo.2620545](https://doi.org/10.5281/zenodo.2620545)
- Timmes, F. X. 2000, ApJ, 528, 913, doi: [10.1086/308203](https://doi.org/10.1086/308203)
- Timmes, F. X. 2019
- Timmes, F. X., & Swesty, F. D. 2000, ASTROPHYS J SUPPL S, 126, 501, doi: [10.1086/313304](https://doi.org/10.1086/313304)
- Turk, M. J., Smith, B. D., Oishi, J. S., et al. 2010, ApJS, 192, 9, doi: [10.1088/0067-0049/192/1/9](https://doi.org/10.1088/0067-0049/192/1/9)
- van der Walt, S., Colbert, S. C., & Varoquaux, G. 2011, Comput. Sci. Eng., 13, 22, doi: [10.1109/mcse.2011.37](https://doi.org/10.1109/mcse.2011.37)
- Wallace, R. K., Woosley, S. E., & Weaver, T. A. 1982, ApJ, 258, 696, doi: [10.1086/160119](https://doi.org/10.1086/160119)
- Weinberg, N. N., & Bildsten, L. 2007, ApJ, 670, 1291, doi: [10.1086/522111](https://doi.org/10.1086/522111)
- Weinberg, N. N., Bildsten, L., & Schatz, H. 2006, ApJ, 639, 1018, doi: [10.1086/499426](https://doi.org/10.1086/499426)
- Woosley, S. E., Wunsch, S., & Kuhlen, M. 2004a, ApJ, 607, 921, doi: [10.1086/383530](https://doi.org/10.1086/383530)
- Woosley, S. E., Heger, A., Cumming, A., et al. 2004b, The Astrophysical Journal Supplement Series, 151, 75, doi: [10.1086/381533](https://doi.org/10.1086/381533)
- Yakovlev, D. G., Gasques, L. R., Afanasjev, A. V., Beard, M., & Wiescher, M. 2006, Physical Review C, 74, doi: [10.1103/physrevc.74.035803](https://doi.org/10.1103/physrevc.74.035803)
- Zhang, W., Almgren, A., Beckner, V., et al. 2019, JOSS, 4, 1370, doi: [10.21105/joss.01370](https://doi.org/10.21105/joss.01370)
- Zingale, M., Eiden, K., & Katz, M. 2023, arXiv e-prints, arXiv:2303.17077, doi: [10.48550/arXiv.2303.17077](https://doi.org/10.48550/arXiv.2303.17077)
- Zingale, M., Katz, M. P., Bell, J. B., et al. 2019, ApJ, 886, 105, doi: [10.3847/1538-4357/ab4e1d](https://doi.org/10.3847/1538-4357/ab4e1d)
- Zingale, M., Katz, M. P., Nonaka, A., & Rasmussen, M. 2022, The Astrophysical Journal, 936, 6, doi: [10.3847/1538-4357/ac8478](https://doi.org/10.3847/1538-4357/ac8478)
- Zingale, M., Katz, M. P., Willcox, D. E., & Harpole, A. 2021, Research Notes of the AAS, 5, 71, doi: [10.3847/2515-5172/abf3cb](https://doi.org/10.3847/2515-5172/abf3cb)